The effect of electron and hole doping on the thermoelectric properties of shandite-type Co3Sn2S2

The effect of electron and hole doping on the thermoelectric properties of shandite-type $Co_3Sn_2S_2$

Panagiotis Mangelis,[a] Paz Vaqueiro,[a] Jean-Claude Jumas,[b] Ivan da Silva,[c] Ronald I. Smith[c] and Anthony V. Powell[*a]

a. Department of Chemistry, University of Reading, Whiteknights, Reading RG6 6AD, UK.

b. Institut Charles Gerhardt, UMR 5253, Université Montpellier II, F-34095, Montpellier 5, France.

c. STFC, Rutherford Appleton Laboratory, ISIS Facility, Didcot OX11 0QX, UK.

Corresponding author:

Prof. Anthony V. Powell

E-mail: a.v.powell@reading.ac.uk

Tel: +44 118 378 6585

Fax: +44 131 451 8034

Abstract:

Electron and hole doping in $Co_3Sn_2S_2$, through chemical substitution of cobalt by the neighbouring elements, nickel and iron, affects both the structure and thermoelectric properties. Electron doping to form $Co_{3-x}Ni_xSn_2S_2$ ($0 \leq x \leq 3$) results in an expansion of the kagome layer and materials become increasingly metallic as cobalt is substituted. Conversely, hole doping in $Co_{3-x}Fe_xSn_2S_2$ ($0 \leq x \leq 0.6$) leads to a transition from metallic to *n*-type semiconducting behaviour at $x = 0.5$. Iron substitution induces a small increase in the separation between the kagome layers and improves the thermoelectric performance. Neutron diffraction data reveal that substitution occurs at the Co 9(*d*) site in a disordered fashion. Mössbauer spectroscopy reveals two iron environments with very different isomer shifts, which may be indicative of a mixed-valence state, while Sn exhibits an oxidation state close to zero in both series. $Co_{2.6}Fe_{0.4}Sn_2S_2$ exhibits a maximum figure-of-merit, ZT = 0.2 at 523 K while $Co_{2.4}Fe_{0.6}Sn_2S_2$ reaches a power factor of 10.3 μW cm^{-1} K^{-2} close to room temperature.

Keywords: Sulfides; Shandite; Neutron diffraction; Electrical properties; Thermal conductivity; Thermoelectric materials.

1. Introduction

The increased requirements for energy consumption as well as the demand for reducing the environmental impact of CO_2 emissions have led to an explosion of research on sustainable energy technologies and new materials for energy harvesting. Thermoelectric (TE) devices are able to provide considerable energy savings when applied in technologies where waste heat can be exploited to create the necessary temperature gradient. The great benefit is that heat is converted directly to electrical power and consequently it is a sustainable energy technology, which may contribute to reducing carbon emissions. From the point of view of materials, [1] high TE performance requires the unusual combination of a high electrical conductivity (σ), usually associated with metallic phases, together with a high Seebeck coefficient (S) and low thermal conductivity (κ), characteristics of non-metallic materials, in order to maximise the figure-of-merit, $ZT = S^2\sigma T/\kappa$. Commercial TE materials for low-temperature applications ($T \leq 473$ K) are generally alloys of Bi_2Te_3 and Sb_2Te_3 which exhibit $ZT \approx 1$ at room temperature [2]. However, these materials are unsuitable for large-scale applications due to the scarcity of tellurium (terrestrial abundance of Te ≈ 0.001 ppm) [3]. Considerable effort is therefore being directed towards the discovery of alternative low-cost materials containing earth-abundant elements. Candidate TE materials containing earth-abundant elements which have attracted great interest are sulphides and selenides, including A_xTiS_2,[4] PbS and PbSe,[5] Chevrel phases[6] and rare-earth sulphides[7].

Low dimensionality is a promising approach to improve the TE performance of materials owing to the more structured density of states (DOS)[8] that results. According to the Mott relation,[9] the Seebeck coefficient is proportional to the

derivative of the DOS at the Fermi level (E_F). Therefore, tuning E_F to sharply-structured regions of the DOS can lead to an enhancement of the Seebeck coefficient.

This search for materials with a highly structured DOS in the region of E_F has led to the investigation of pseudo two-dimensional mixed-metal sulphides of general formula $M_3M'_2S_2$ that contain transition-series elements (M = Co, Ni, Fe, Rh, Pd) together with elements from group III and IV (M' = Sn, In, Pb, Tl), which crystallise in the shandite structure (Fig. 1).

An unusual combination of a metal-like electrical conductivity and a Seebeck coefficient of *ca*. -48 μV K^{-1} at 300 K [10] has led to a high level of interest in the shandite-type ferromagnet $Co_3Sn_2S_2$ (T_C = 176 K). This phase has been described as a type I_A half-metal;[11] a view which is confirmed by photoemission studies [12]. Band structure calculations indicate the region around the Fermi level is composed predominantly of Co 3*d* states with small contributions from Sn 5*p* and S 3*p* states. The resulting sharp peak in the DOS at E_F may contribute to the relatively high Seebeck coefficient [13].

Magnetic susceptibility measurements reveal that nickel substitution in $Co_{3-x}Ni_xSn_2S_2$ ($0 \leq x \leq 3$) suppresses the ferromagnetic order at $x > 0.2$ [14]. Band structure calculations [15] indicate that the band gap of $Ni_3Sn_2S_2$ is moved to higher energies within 3*d* states. Mössbauer and XPS experiments have shown that $Ni_3Sn_2S_2$ is metallic with the formal configuration: $(Ni^0)_3(Sn(1)^{2+})(Sn(2)^{2+})(S^{2-})_2$ [16]. There is contradictory evidence for oxidation states in the cobalt end-member phase, $Co_3Sn_2S_2$. ^{119}Sn Mössbauer spectroscopy [17] appears to rule out Sn(II) and Sn(IV) states, while Umetani *et al*.[18] suggest cobalt is present as a mixture of Co(0) and Co(II). However, X-ray photoelectron spectroscopy data for $Co_3Sn_{2-x}In_xS_2$ indicate a zero valent state for cobalt, and for sulfur, an oxidation state which approaches zero,[19]

with Bader charge analysis from DFT calculations indicating a net negative charge of ca. 0.7 associated with sulfur. In addition, ^{119}Sn Mössbauer spectra reveal an oxidation state for the two tin atoms which is close to zero.

Synthesis of $Co_{3-x}Fe_xSn_2S_2$ at high pressures and temperatures leads to single phase behaviour that extends to x = 1 [20]. At ambient pressure, growth of single crystals of $Co_{3-x}Fe_xSn_2S_2$ with a maximum x = 0.53 has been reported [21]. The Curie temperature, T_C, decreases with iron content in a similar fashion to that observed in indium-substituted shandites, suggesting that the electron count is a key parameter in determining the magnetic ground state of the material [22].

There are very few studies of the TE properties of shandite phases. Corps *et al.* [23] have demonstrated that substitution of tin by indium in $Co_3Sn_{2-x}In_xS_2$ enhances the TE performance by tuning E_F within narrow *d*-bands. This results in ZT = 0.2 at room temperature in $Co_3Sn_{1.15}In_{0.85}S_2$, which represents an almost 3-fold increase over that of $Co_3Sn_2S_2$. Recently the effect of Se substitution on the TE properties of Co_3SnInS_2 at low temperatures has been examined [24]. The simultaneous substitution of indium and selenium induces metallic behaviour and a decrease in resistivity without suppression of the Seebeck coefficient. Here, we describe how chemical substitution at the cobalt site of $Co_3Sn_2S_2$ may be used to manipulate the electronic properties and hence the TE behaviour by tuning the position of E_F within the narrow bands in the vicinity of E_F.

2. Experimental

All samples of general formula $Co_{3-x}A_xSn_2S_2$ (A = Ni ($0 \leq x \leq 3$), Fe ($0 \leq x \leq 0.6$)) were prepared by high temperature synthesis. Appropriate mixtures of elemental nickel (Alfa Aesar, powder, 99.9%), cobalt (Alfa Aesar, powder, 99.8%), tin (Sigma-Aldrich, powder, ≥ 99%), iron (Sigma-Aldrich, powder, 99.9%) and sulphur (Sigma-

Aldrich, flakes, 99.99%) were ground using an agate pestle and mortar. The resulting powders were sealed under vacuum (10^{-4} mbar) into fused silica tubes prior to heating at 500 ˚C and 700 ˚C, each for 48 h, with an intermediate regrinding. The heating/cooling rate was 0.5 ˚C min^{-1}.

Initial structural characterization was carried out by powder X-ray diffraction using a Bruker D8 Advance diffractometer (Ge-monochromated Cu $K\alpha_1$, λ = 1.5406 Å and a LynxEye linear detector). Powder neutron diffraction experiments on both series, $Co_{3-x}Ni_xSn_2S_2$ ($0 \leq x \leq 3$) and $Co_{3-x}Fe_xSn_2S_2$ ($0 \leq x \leq 0.6$), were conducted at the ISIS facility, Rutherford Appleton Laboratory, UK, using the GEM diffractometer. Powdered samples were placed in thin-walled cylindrical vanadium cans and data collected at room temperature. Multibank Rietveld refinements were performed with the GSAS software package using data from banks centred at 2θ = 154°, 91°, 63° and 35°. The initial structural model in space group $R\bar{3}m$ used lattice parameters determined from powder X-ray diffraction data and atomic coordinates of the cobalt end-member phase [10].

^{119}Sn and ^{57}Fe Mössbauer spectroscopic data were recorded in transmission mode and in constant acceleration mode using as sources ^{119}Sn embedded in a $CaSnO_3$ matrix and ^{57}Co (Rh), respectively. The velocity scales were calibrated with the magnetic sextet of a high-purity α-Fe foil as the reference absorber, using ^{57}Co (Rh) as the source. The absorbers containing 1 – 2 mg cm^{-2} of ^{119}Sn or 0.1 - 0.2 mg cm^{-2} of ^{57}Fe were prepared inside an argon-filled glove box, by mixing the powder samples with Apiezon grease held between two Kapton films. The sample holder was sealed to prevent air contact. The hyperfine parameters δ (isomer shift) and ΔE_q (quadrupole splitting) were determined by fitting Lorentzian profiles to the experimental spectra, using a least-squares method. The resulting errors in the hyperfine parameters are

found to be smaller than 0.01 mm s^{-1} for the different $Co_{3-x}Fe_xSn_2S_2$ compounds. The isomer shift values for the ^{119}Sn spectra are given relative to δ values of a $BaSnO_3$ spectrum recorded at room temperature, whilst the ^{57}Fe data are expressed relative to α-Fe.

Samples were consolidated by hot-pressing for 25 min at 60 bar and 995 K, under a nitrogen atmosphere, using a hot press constructed in-house. All samples were ball-milled at 350 rpm for 1 hour prior to consolidation. The densities of the resulting pellets, determined by the Archimedes method using an Adam PW184 balance, are ca 98% of the crystallographic value. Thermal diffusivity measurements were performed using a Netzsch LFA 447 Nanoflash instrument. Measurements were conducted in 25 K increments, over the temperature range $300 \leq T / K \leq 525$, on circular pellets (diameter: 12.5 – 12.6 mm; thickness: 1.8 – 1.9 mm) coated with graphite. Pyroceram 9606 was used as a reference for the determination of the heat capacity. The electrical resistivity and Seebeck coefficient were determined using a Linseis LSR3-800 over the temperature range $300 \leq T/K \leq 625$, under a temperature gradient of 10 K. Measurements were conducted under a partial pressure of helium, using a current of 100 mA.

3. Results and discussion

Powder X-ray diffraction data confirm that $Co_{3-x}Ni_xSn_2S_2$ exists as a single phase over the entire range of composition ($0 \leq x \leq 3$), crystallising in the space group $R\bar{3}m$. Nickel substitution increases the *a* lattice parameter by *ca.* 1.9%, corresponding to an expansion of the kagome lattice, whilst the *c* lattice parameter is not affected greatly by substitution, exhibiting a broad, weak maximum for x = 2.5. X-ray diffraction data for the series $Co_{3-x}Fe_xSn_2S_2$ reveal that the single phase region extends only to x = 0.6, with impurities of SnS, FeS, and FeSn being identified when attempting to synthesise compositions with higher

levels of substitution. The compositional dependence of lattice parameters is comparable to that in single crystals [21]. By contrast with $Co_{3-x}Ni_xSn_2S_2$, iron substitution results in a negligible composition dependence to the *a* lattice parameter, while the *c* lattice parameter exhibits a slight (~ 0.3 %) increase. The compositional variation of lattice parameters of both series is provided as supplementary material.

Powder neutron diffraction data were used to provide the necessary contrast between Co and Ni/Fe, including the investigation of the possibility of transition-metal ordering or of substitution at Sn/S sites by a transition-metal. The neutron data could be indexed on the basis of the shandite unit cell and examination of data at long d-spacings provide no evidence for a supercell arising from transition-metal ordering. Rietveld refinement confirms that Ni/Fe substitutes at the 9(*d*) site. Refinements in which Ni/Fe was placed at the Sn or S sites failed to reproduce the observed intensities and the refinements were unstable. Representative multibank Rietveld refinements are presented in Fig. 2, with the remaining profiles provided as supplementary material. The refined lattice, atomic and thermal parameters are presented in Table 1 while selected bond lengths and angles are presented as supplementary material.

The substitution of cobalt by nickel increases the electron count by three electrons across the series. $Co_3Sn_2S_2$ has 47 valence electrons which occupy 24 of 31 bands. E_F crosses the half-occupied 24^{th} band which is mainly of Co 3*d* character [11]. According to recent DFT calculations for In substitution, [19] at energies just above E_F the main contribution to the DOS in $Co_3Sn_2S_2$ arises from Co-based d_{xy} and d_{x2-y2} orbitals. These states contribute primarily to the in-plane interactions, which our previous investigations [19] suggest are anti-bonding in character. The increased electron count on substitution results in the progressive filling of the 24^{th} and 25^{th} bands, consistent with the DOS calculations of $Ni_3Sn_2S_2$ by Gütlich *et al.*,[16] which

confirm that the *d*-orbitals in the other end-member phase $Ni_3Sn_2S_2$ are fully occupied. The addition of electrons to d_{xy}/d_{x2-y2} states increases the antibonding character of M–Sn(2) interactions, thereby weakening the bonds within the kagome layers, leading to the observed increase in *a* lattice parameter. This is consistent with bond distances obtained by Rietveld refinement, which are provided as supplementary material.

Analysis of neutron diffraction data of two iron substituted samples, $Co_{2.7}Fe_{0.3}Sn_2S_2$ and $Co_{2.4}Fe_{0.6}Sn_2S_2$, reveal that the decrease in *a* lattice parameter is offset by the increase in *c* lattice parameter, leading to an effectively constant volume (Table 1). Previously published DFT calculations for $Co_{3-x}Fe_xSn_2S_2$ [20] indicate a continuous shift of valence band and E_F to lower energies as cobalt is replaced by iron. The calculated DOS for x = 1 shows a clear separation of valence bands from the conduction band and the location of E_F in the band gap, indicating that $Co_2FeSn_2S_2$ is non-metallic [20]. ^{119}Sn Mössbauer spectroscopic data for $Co_{3-x}Fe_xSn_2S_2$ ($0 < x \leq 0.6$), provided as supplementary material, reveal that iron substitution does not affect the local electronic structure of the two tin sites, Sn(1) and Sn(2). Throughout the series, the isomer shift of Sn(2), located in the kagome layer, lies in the narrow range of 2.11 - 2.13 mm s^{-1}, while that of Sn(1) in the interlayer sites is in the range 2.16 – 2.18 mm s^{-1}. The hyperfine parameters of the two crystallographically-distinct tin atoms are similar to those reported by Corps et al., [19] indicating that the near zero oxidation state previously established for Sn(1) and Sn(2) atoms in $Co_3Sn_2S_2$ [19,25] is retained in $Co_{3-x}Fe_xSn_2S_2$ ($0 < x \leq 0.6$).

^{57}Fe Mössbauer spectroscopic data for $Co_{3-x}Fe_xSn_2S_2$ ($0 < x \leq 0.6$) show two doublets throughout the series. Representative ^{57}Fe data are presented in Fig. 3, with the remaining spectra provided as supplementary material. The hyperfine parameters are presented in Table 2. The more intense doublet with a relative contribution of *ca*. 80%,

exhibits an isomer shift in the range 0.40 - 0.44 mm s^{-1} and a quadrupole splitting of 0.62 – 0.63 mm s^{-1}. The corresponding ranges for the weaker doublet (*ca*. 20%) are 0.10 - 0.27 mm s^{-1} and 0.16 – 0.44 mm s^{-1} respectively. The observation of two doublets is perhaps surprising given the location of iron at a single crystallographic 9(*d*) site. The contrast between iron and tin provided by neutrons excludes the possibility of the occupation by iron of two crystallographically-distinct sites, through substitution at either tin site, 3(*a*) or 3(*b*). Furthermore, powder X-ray and neutron diffraction data provide no evidence for the presence of impurity phases at a level that would give rise to a signal of the magnitude observed here (*ca*. 20%) for the second doublet. The origin of two doublets in the ^{57}Fe Mössbauer spectra must therefore lie in different local environments of the iron substituent. A given iron centre at the 9(*d*) site within the kagome layer has two tin and four transition-metal nearest neighbours. As a result of the substitutional disorder, established by powder neutron diffraction, the latter may be either iron or cobalt. Calculations suggest that at low levels of substitution, the probability of an iron centre being surrounded by four cobalt neighbours in addition to the two tin neighbours is *ca*. 0.84, with the next most likely environment, in which a single cobalt is replaced by iron in the local coordination environment, having a probability of *ca* 0.15. This suggests that the more intense doublet at δ = 0.40 – 0.44 mm s^{-1} can be assigned to iron atoms surrounded only by cobalt and tin, whilst the weaker feature is associated with iron atoms that have iron near neighbours. The ratio of the contributions of the two doublets is in good agreement with the calculated relative probabilities at $x \leq 0.2$. At higher iron contents the ratio of the intensities of the doublets deviates from that expected on probability grounds, suggesting that the distribution of iron atoms in the kagome layer is no longer purely statistical.

The values of the isomer shift for the doublet at $\delta \approx 0.4$ mm s^{-1} compare favourably with that of the structurally related intermetallic, FeSn (0.41 mm s^{-1}),[26] which contains similar kagome layers to those in $Co_{3-x}Fe_xSn_2S_2$. These values are similar to those reported for $KFeS_2$ (0.42,[27] 0.43 [28] mm s^{-1}) and assigned to Fe^{3+}. The assignment of the second doublet is less clear since isomer shifts for iron in different oxidation and spin states show considerable overlap. What is clear is that the isomer shift of the weaker doublet is displaced to markedly lower values, suggesting an increase in electron density at the nucleus. This may be associated with Fe-Fe near-neighbour interactions. Mössbauer data for the marcasite phase, FeS_2, yields isomer shifts 0.23 [29] and 0.277 [30] mm s^{-1} for Fe^{2+}, whilst a comparable isomer shift of 0.24 mm s^{-1} has been observed for the ferric ions in natural single crystals of α-$CuFeS_2$ [31] and the chalcopyrite-related $TlFeS_2$ exhibits [32] an isomer shift of 0.18 mm s^{-1}. Similarly, Benedetto et al [33] have suggested that in the solid solution Cu_2FeSnS_4-Cu_2ZnSnS_4, Fe^{3+} ions arising from defect formation are responsible for features in the Mössbauer spectrum with isomer shifts in the range 0.25 – 0.30 mm s^{-1}, with those arising from the majority tetrahedral Fe^{3+} species, being observed at much higher isomer shifts of *ca*. 0.6 mm s^{-1}. Although the data presented here could indicate a mixed Fe^{2+}/Fe^{3+} oxidation state in the substituted shandite phases, perhaps the principal conclusion is that iron is present in a non-zero formal oxidation state and is located in two different local environments. Unfortunately magnetic measurements [24] provide no additional information on the formal oxidation states as materials in the series $Co_{3-x}Fe_xSn_2S_2$ behave as itinerant ferromagnets, with small effective magnetic moments of 0.61-0.45 μ_B.

The electrical resistivity for all samples in the $Co_{3-x}Ni_xSn_2S_2$ series increases as a function of temperature, indicating metallic behaviour (Fig. 4). The increase in nickel

content markedly reduces the electrical resistivity of the material. It is notable that $Ni_3Sn_2S_2$ reaches a resistivity as low as 0.04 mΩ cm which is almost an order of magnitude lower than that of $Co_3Sn_2S_2$. Seebeck coefficients (Fig. 4) are negative throughout the composition range $0 \leq x \leq 3$, indicating that electrons are the principal charge carriers and all compositions are *n*-type materials. The absolute value of the Seebeck coefficient, $|S|$ increases almost linearly with temperature, consistent with the metallic behaviour indicated by the resistivity data. The absolute value of the Seebeck coefficient decreases with increasing Ni content, exhibiting a minimum value at x = 2.5. The simultaneous decrease of resistivity and $|S|$ on substitution leads to an overall reduction in the power factor of the material (Fig. 4).

Hole doping results in markedly different behaviour (Fig. 5). Electrical resistivity increases with increasing iron content. Up to x = 0.4, ρ(T) exhibits a metallic temperature dependence, whilst for $x \geq 0.5$, materials exhibit semiconducting behaviour. The Seebeck coefficient indicates *n*-type behaviour throughout the composition range $0 \leq x \leq 0.6$. The absolute value of the Seebeck coefficient, $|S|$, increases with iron content (Fig. 5), with the most iron-rich sample, $Co_{2.4}Fe_{0.6}Sn_2S_2$, exhibiting a value 66% higher than the undoped phase at room temperature. The increase in Seebeck coefficient across the series outweighs the reduction in electronic conductivity, resulting in an increase of the power factor (Fig. 5), which reaches 10.3 $\mu W\ cm^{-1}\ K^{-2}$ for $Co_{2.4}Fe_{0.6}Sn_2S_2$ close to room temperature. This corresponds to an increase of 29% from that of the end-member $Co_3Sn_2S_2$. The substitution of cobalt by iron reduces the charge carrier density, and the resulting depopulation of the *d*-band, in the vicinity of E_F, shifts E_F downwards to a region of the DOS where the greater curvature and hence larger derivative of the DOS, may be responsible for the increase in $|S|$ [9].

The thermal conductivity (κ) of $Co_{3-x}Ni_xSn_2S_2$ (Fig. 6) remains almost constant up to a composition of x =1, whilst for higher nickel contents there is a rise in thermal conductivity which becomes particularly marked as x = 3 is approached. The electronic contribution, κ_{el}, was determined using the Wiedemann-Franz law ($L_0 = 2.44\times10^{-8}$ W Ω K^{-2}), and the lattice contribution, κ_L, as the difference between κ and κ_{el}. This analysis presented as supplementary material indicates that the total thermal conductivity is determined predominantly by the electronic contribution, which rises with Ni content, whilst the lattice contribution is almost independent of composition. This is consistent with an increase in charge carrier concentration on nickel substitution and the absence of any appreciable mass fluctuation scattering owing to the similar atomic masses of nickel and cobalt.

The thermal conductivity of $Co_{3-x}Fe_xSn_2S_2$ falls on substitution by iron, (Fig. 7); the lowest value at room temperature (at x = 0.5) showing a 32% reduction from that of $Co_3Sn_2S_2$. The electronic contribution, κ_{el}, at constant temperature decreases with increasing iron content, whilst κ_L is effectively compositionally invariant, consistent with the absence of mass fluctuation scattering for elements whose atomic masses differ by only 1 amu.

Electron doping through substitution of cobalt by nickel leads to a marked decrease in ZT (Fig. 6), principally due to the reduction in $|S|$. By contrast, in the case of iron substitution the combination of a reduction in thermal conductivity and increase in the magnitude of the Seebeck coefficient is sufficient to offset the increase in resistivity, resulting in an increase in the figure-of-merit of $Co_{3-x}Fe_xSn_2S_2$ ($0 \leq x \leq 0.6$) (Fig. 7). The greatest differences in ZT are observed at low temperatures. It is remarkable that at 350 K, $Co_{2.5}Fe_{0.5}Sn_2S_2$ exhibits ZT = 0.11, which is double that of $Co_3Sn_2S_2$. At 525 K, the maximum value of 0.2 is shown by $Co_{2.6}Fe_{0.4}Sn_2S_2$ and corresponds to an increase of *ca.* 22% from that of $Co_3Sn_2S_2$.

This improvement of TE performance in $Co_{3-x}Fe_xSn_2S_2$ ($0 \leq x \leq 0.6$) offers a promising avenue for future optimization of the thermoelectric properties of shandite-related phases. To date chemical substitution in $Co_3Sn_2S_2$ has focused on the main-group metal and anion sites. Our previous study [23] of $Co_3Sn_{2-x}In_xS_2$ revealed an enhancement of TE performance leading to power factors in the range 12 – 14 $\mu W cm^{-1} K^{-2}$ at room temperature. The present work reveals a similarly high power factor of 10.3 $\mu W\ cm^{-1}\ K^{-2}$ for $Co_{2.4}Fe_{0.6}Sn_2S_2$ at similar temperatures. Moreover, substitution by transition metals at the cobalt site also obviates the need for the relatively costly element, indium. It is notable that $Co_{2.5}Fe_{0.5}Sn_2S_2$ exhibits a higher ZT close to room temperature than that of other promising sulphides including Bi_2S_3, [34] $Pb_{0.0975}Na_{0.025}S$, [5] $NdGdS_3$, [7] $Cu_xMo_6S_8$, [35] which exhibit maximum values of ZT at elevated temperatures ($T \geq 700$ K).

4. Conclusions

In conclusion, cobalt in $Co_3Sn_2S_2$ may be substituted by its neighbouring elements, Ni and Fe, to achieve electron and hole doping. The single phase region extends over the entire range of composition ($0 \leq x \leq 3$) in the case of nickel substitution, whereas that for iron is more restricted ($0 \leq x \leq 0.6$). Neutron data demonstrate that that substitution of cobalt by both iron and nickel occurs in a disordered fashion throughout the two series. ^{57}Fe Mössbauer spectra for materials $Co_{3-x}Fe_xSn_2S_2$ ($0 \leq x \leq 0.6$), show two distinct sub spectra, which arise from the differences in the local environment of iron atoms at the disordered 9(*d*) site. ^{119}Sn Mössbauer data show that the two tin sites are not affected by iron substitution and retain the zero valent state. Nickel substitution increases the metallic character of the material, consistent with the results of DFT calculations for the end-member phases ($M_2Sn_2S_2$, M = Co, Ni), [16,19] and there is a

concomitant decrease in Seebeck coefficient. This is principally responsible for the overall reduction of ZT with increasing nickel content. By contrast, hole-doping through the introduction of iron, results in an improvement in TE performance. Iron substitution leads to a transition to *n*-type semiconducting behaviour at x= 0.5, consistent with DFT calculations [20]. The observed increase in |*S*| may indicate that E_F is shifted to a region of the DOS in which there are more pronounced discontinuities. This increase in |*S*|, in combination with the reduction of thermal conductivity, contributes to the rise in ZT: $Co_{2.6}Fe_{0.4}Sn_2S_2$ exhibiting the maximum value of ZT = 0.2 at 523 K.

Acknowledgements

The authors would like to thank EPSRC and the University of Reading for financial support for P.M., and for access to the Chemical Analysis Facility for powder X-ray diffraction measurements. The authors also thank the STFC (Science and Technology Facilities Council) for the neutron beam time allocation at the ISIS Facility.

References

[1] P. Vaqueiro, A. V. Powell, Recent developments in nanostructured materials for high-performance thermoelectrics, J. Mater. Chem., 20 (2010) 9577-9584.

[2] G. J. Snyder, E. S. Toberer, Complex thermoelectric materials, Nat. Mater. 7 (2008) 105-114.

[3] P. A. Cox, The Elements: Their Origin, Abundance, and Distribution, Oxford University Press, Oxford, 1989.

[4] E. Guilmeau, Y. Bréard, A. Maignan, Transport and thermoelectric properties in Copper intercalated TiS_2 chalcogenide, Appl. Phys. Lett. 99 (2011) 052107.

[5] L.-D. Zhao, J. He, C.-I. Wu, T. P. Hogan, X. Zhou, C. Uher, V. P. Dravid, M. G. Kanatzidis, Thermoelectrics with earth abundant elements: high performance p-type PbS nanostructured with SrS and CaS, J. Am. Chem. Soc., 134 (2012) 7902-7912.

[6] A. M. Schmidt, M. A. McGuire, F. Gascoin, G. J. Snyder, F. J. DiSalvo, Synthesis and thermoelectric properties of $(Cu_yMo_6Se_8)_{1-x}(Mo_4Ru_2Se_8)_x$ alloys, J. Alloys Compd. 431 (2007) 262-268.

[7] M. Ohta, T. Kuzuya, H. Sasaki, T. Kawasaki, S. Hirai, Synthesis of multinary rare-earth sulfides $PrGdS_3$, $NdGdS_3$, and $SmEuGdS_4$, and investigation of their thermoelectric properties, J. Alloys Compd. 484 (2009) 268-272.

[8] L. D. Hicks, M. S. Dresselhaus, Effect of quantum-well structures on the thermoelectric figure of merit, Phys. Rev. B Condens. Matter Mater. Phys. 47 (1993) 12727-12731.

[9] N. F. Mott, E. A. Davis, Electronic Processes in Non-Crystalline Materials, Clarendon Press, Oxford, 1979.

[10] P. Vaqueiro, G. G. Sobany, A powder neutron diffraction study of the metallic ferromagnet $Co_3Sn_2S_2$, Solid State Sci. 11 (2009) 513-518.

[11] R Weihrich, I. Anusca, Half antiperovskites. III - Crystallographic and electronic structure effects in $Sn_{2-x}In_xCo_3S_2$, Z. Anorg. Allg. Chem. 632 (2006) 1531-1537.

[12] M. Holder, Yu. S. Dedkov, A. Kade, H. Rosner, W. Schnelle, A. Leithe-Jasper, R. Weihrich, S. L. Molodtsov, Photoemission study of electronic structure of the half-metallic ferromagnet $Co_3Sn_2S_2$, Phys. Rev. B Condens. Matter Mater. Phys. 79 (2009) 205116.

[13] Y.S. Dedkov, M. Holder, S.L. Molodtsov and H. Rosner, Electronic structure of shandite $Co_3Sn_2S_2$, J. Phys.: Conf. Ser 100 (2008) 072011.

[14] T. Kubodera, H. Okabe, Y. Kamihara, M. Matoba, Ni substitution effect on magnetic and transport properties in metallic ferromagnet $Co_3Sn_2S_2$, Physica B 378 – 380 (2006) 1142-1143.

[15] R. Weihrich, I. Anusca, M. Zabel, Half-antiperovskites: Structure and type-antitype relations of shandites $M_{3/2}AS$ (M = Co, Ni; A = In, Sn), Z. Anorg. Allg. Chem. 631 (2005) 1463-1470.

[16] P. Gütlich, K.-J. Range, C. Felser, C. Schultz-Münzenberg, W. Tremel, D. Walcher, M. Waldeck, The valence states of nickel, tin, and sulfur in the ternary chalcogenide $Ni_3Sn_2S_2$-XPS, ^{61}Ni and ^{119}Sn Mossbauer investigations and band structure calculations, Angew. Chem., Int. Ed. 38 (1999) 2381-2384.

[17] J. Rothballer, F. Bachhuber, F. Pielnhofer, F. M. Schappacher, R. Pöttgen, R. Weihrich, Effect of In-Sn Ordering on Semiconducting Properties in $InSnCo_3S_2$ - X-ray, ^{119}Sn Mossbauer Spectroscopy, and DFT Studies, Eur. J. Inorg. Chem. (2013) 248-255.

[18] A. Umetani, E. Nagoshi, T. Kubodera, M. Matoba, Electronic and magnetic nature of shandite-type $A_2Co_3S_2$ (A = Sn, In) Physica B 403 (2008) 1356-1358.

[19] J. Corps, P. Vaqueiro, A. Aziz, R. Grau-Crespo, W. Kockelmann, J.C. Jumas, A.V. Powell, Interplay of metal-atom ordering, Fermi level tuning and thermoelectric properties in cobalt shandites $Co_3M_2S_2$ (M = Sn, In) Chem. Mater. 27 (2015) 3946-3956.

[20] Y. Sakai, R. Tanakadate, M. Matoba, I. Yamada, N. Nishiyama, T. Irifune, K. Funakoshi, T. Kunimoto, Y. Higo and Y. Kamihara, Magnetic Properties of Shandite-Phase $Co_{3-x}Fe_xSn_2S_2$ (x=0-1.0) Obtained with High Pressure Synthesis, J. Phys. Soc. Jap. 84 (2015) 044705.

[21] M. A. Kassem, Y. Tabata, T. Waki, H. Nakamura, Structure and magnetic properties of flux grown single crystals of $Co_{3-x}Fe_xSn_2S_2$ shandites, J. Solid State Chem. 233 (2016), 8-13.

[22] M. A. Kassem, Y. Tabata, T. Waki, H. Nakamura, Quasi-Two-Dimensional Magnetism in Co-Based Shandites J. Phys. Soc. Jpn. 85 (2016) 064706.

[23] J. Corps, P. Vaqueiro, A.V. Powell, $Co_3M_2S_2$ (M = Sn, In) Shandites as Tellurium-Free Thermoelectrics, J. Mater. Chem. A, 1 (2013) 6553-6557.

[24] M. Fujioka, T. Shibuya, J. Nakai, K. Yoshiyasu, Y. Sakai, Y. Takano, Y. Kamihara, M. Matoba, The effect of simultaneous substitution on the electronic band structure and thermoelectric properties of Se-doped Co_3SnInS_2 with the Kagome lattice, Solid State Commun., 199 (2014) 56-60.

[25] P. E. Lippens, Interpretation of the ^{119}Sn Mossbauer isomer shifts in complex tin chalcogenides Phys. Rev. B Condens. Matter Mater. Phys. 60 (1999) 4576-4586.

[26] E. Fluck, W. Kerler, W. Neuwirth, The Mössbauer Effect and its Significance in Chemistry, Angew. Chem. Int. Ed. 2 (1963) 277-287.

[27] N. N. Greenwood, H. J. Whitfield, Mössbauer effect studies on cubanite ($CuFe_2S_3$) and related iron sulphides J. Chem. Soc. (A) (1968) 1697-1699.

[28] L. Häggström, T Ericsson, R. Wäppling, E. Karlsson, K. Chandra, Mössbauer studies of the isostructural compounds FeGe, FeSn and CoSn, J. Phys. Colloq. 35(C6) (1974) 603-607.

[29] R. Garg. E.Galvao da Silva, Y.S. Liu, V. K. Garg, Mössbauer investigation of iron disulphide (marcasite), Solid State Commun. 50 (1984) 1-2.

[30] A. A. Temperly, H. W. Lefevre, The Mössbauer effect in marcasite structure iron compounds, J. Phys. Chem. Solids 27 (1966) 85-92.

[31] C. Boekema, A. M. Krupski, M. Varasteh, K. Parvin, F. van Til, F. van der Woude, G. A. Sawatzki, Cu and Fe valence states in $CuFeS_2$, J. Magn. Magn. Mater. 272 (2004) 559-561.

[32] K. Forcher, W. Lottermoiser, G. Amthauer, Mössbauer study of raguinite, $TlFeS_2$, und thalcusite, $Cu_3T1_2FeS_4$ Neu. Jb. Mineral, Abh. 160 (1988) 25-28.

[33] F. Di Benedetto, G. P. Bernardini, D. Borrini, W. Lottermoser, G. Tippelt, G. Amthauer, ^{57}Fe- and ^{119}Sn-Mossbauer study on stannite (Cu_2FeSnS_4)-kesterite (Cu_2ZnSnS_4) solid solution, Phys. Chem. Miner. 31 (2005) 683-690.

[34] D. Guo, C. Hu and C. Zhang, First-principles study on doping and temperature dependence of thermoelectric property of Bi_2S_3 thermoelectric material, Mater. Res. Bull. 48 (2013) 1984-1988.

[35] M. Ohta, H. Obara and A. Yamamoto, Preparation and Thermoelectric Properties of Chevrel-Phase $Cu_xMo_6S_8$ ($2.0 \leq x \leq 4.0$), Mater. Trans. 50 (2009) 2129-2133.

Table 1 Refined parameters for $Co_{3-x}Ni_xSn_2S_2$ ($0 \leq x \leq 3$) and $Co_{3-x}Fe_xSn_2S_2$ ($0 \leq x \leq 0.6$) using neutron diffraction data, collected at room temperature. Space group $R\bar{3}m$. Atomic coordinates: *M* (*M* = Co, Ni, Fe) 9(*d*) (½, ½, ½), Sn(1) 3(*a*) (0, 0, 0), Sn(2) 3(*b*) (0, 0, ½), S 6(*c*) (0, 0, z).

$Co_{3-x}Ni_xSn_2S_2$ ($0 \leq x \leq 3$)								
x	**a /Å**	**c/Å**	**S(z)**	**V/ Å^3**	***M*** **Uiso/Å^2**	**Sn(1) Uiso /Å^2**	**Sn(2) Uiso /Å^2**	**S Uiso /Å^2**
0	5.37235(4)	13.1972(2)	0.28324(5)	329.869(3)	0.523(8)	0.54(3)	0.60(3)	0.42(2)
0.333	5.37543(4)	13.1878(2)	0.28350(6)	330.012(3)	0.608(7)	0.66(3)	0.72(3)	0.48(2)
0.666	5.38523(5)	13.1931(2)	0.28347(6)	331.349(2)	0.743(5)	0.81(3)	0.89(3)	0.60(2)
1	5.39455(4)	13.1949(2)	0.28353(7)	332.541(2)	0.793(6)	0.88(4)	0.89(4)	0.60(2)
1.333	5.40490(3)	13.2012(1)	0.28332(6)	333.979(2)	0.809(5)	1.00(3)	0.83(3)	0.64(2)
1.666	5.41405(3)	13.1963(1)	0.28320(7)	334.988(4)	0.857(4)	1.03(2)	0.91(2)	0.69(2
2	5.42703(2)	13.20538(9)	0.28288(7)	336.827(2)	0.905(5)	1.04(2)	0.94(2)	0.69(2)
2.333	5.43886(2)	13.20156(8)	0.28254(7)	338.198(2)	0.898(4)	1.01(2)	0.96(2)	0.68(2)
2.666	5.45074(2)	13.19735(9)	0.28221(9)	339.569(2)	0.929(5)	1.03(2)	0.95(2)	0.67(2)
3	5.47092(4)	13.2089(2)	0.2819(2)	342.387(5)	0.930(10)	1.07(4)	0.99(4)	0.65(5)
$Co_{3-x}Fe_xSn_2S_2$ ($0 < x \leq 0.6$)								
0.3	5.36606(7)	13.1955(4)	0.2829(1)	329.055(6)	0.39(1)	0.36(5)	0.42(5)	0.28(3)
0.6	5.36579(6)	13.2115(3)	0.2825(1)	329.421(6)	0.41(1)	0.33(4)	0.40(4)	0.20(3)

Table 2 Isomer Shifts (δ), Quadropole Splitting (Δ), Line Width (Γ) and Contribution of Each Line to the ^{57}Fe Mössbauer Spectra of $Co_{3-x}Fe_xSn_2S_2$ ($0 < x \leq 0.6$).

X	δ (mm s^{-1})	Δ (mm s^{-1})	Γ (mm s^{-1})	Contribution (%)
0.1	0.41(1)	0.62(1)	0.20(5)	85
	0.13(4)	0.44(5)	0.20(5)	15
0.2	0.40 (1)	0.63 (1)	0.24 (5)	76
	0.27 (3)	0.16 (4)	0.24 (5)	24
0.3	0.44 (2)	0.62 (3)	0.28 (1)	81
	0.27 (7)	0.27 (11)	0.28 (1)	19
0.4	0.42 (3)	0.62 (5)	0.26 (9)	80
	0.26 (11)	0.35 (19)	0.26 (9)	20
0.5	0.430 (5)	0.629 (8)	0.20 (4)	84
	0.10 (3)	0.35 (4)	0.20 (4)	16
0.6	0.410 (5)	0.624 (8)	0.27 (4)	84
	0.20 (2)	0.27 (3)	0.27 (4)	16

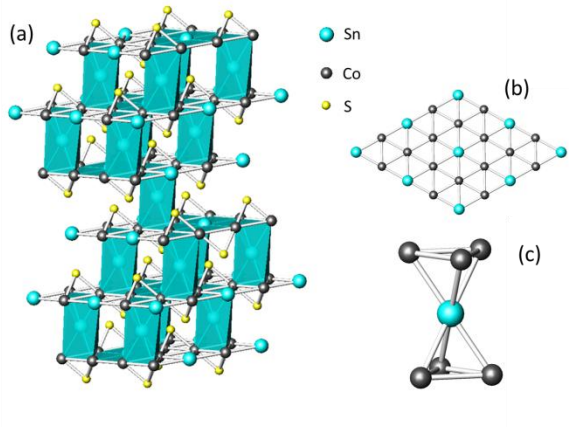

Figure 1 (a) The shandite structure of $Co_3Sn_2S_2$; (b) the Co and Sn(2) atoms form layers with a kagome topology; (c) the Sn(1) atoms are located in interlayer sites and coordinated by six cobalt atoms forming a trigonal antiprismatic configuration (c). The sulphur atoms occupy interlayer positions capping the trigonal shapes of cobalt atoms whether above or below the kagome layers (a).

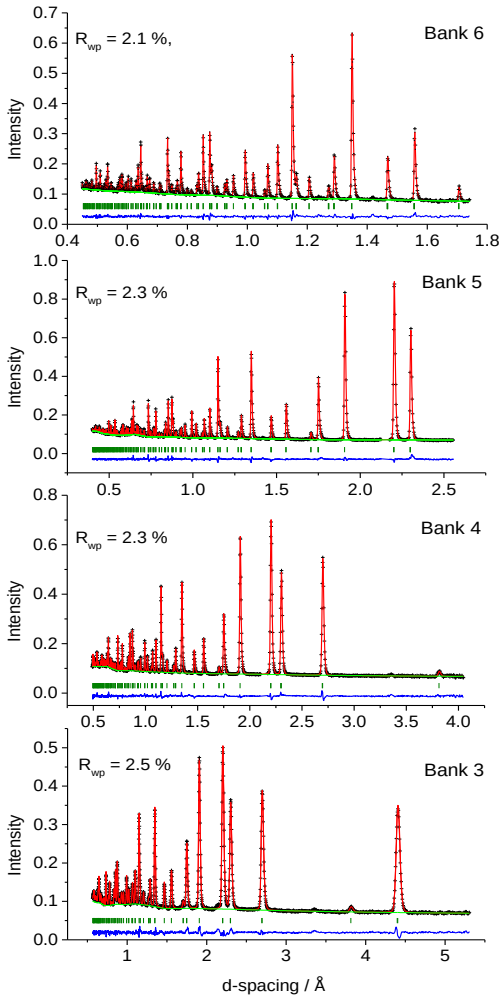

Figure 2 Final observed (black crosses), calculated (red solid lines) and difference (blue bottom line) profiles for refinements of $Co_2NiSn_2S_2$ using neutron diffraction data collected at room temperature from detector banks centred at 2θ = 154°, 91°, 63° and 35° (from top to bottom). Reflection positions are marked and the green line shows the calculated background. Regions containing scattering from the vanadium can have been excluded. The residuals for each bank are indicated (χ^2 = 2.3).

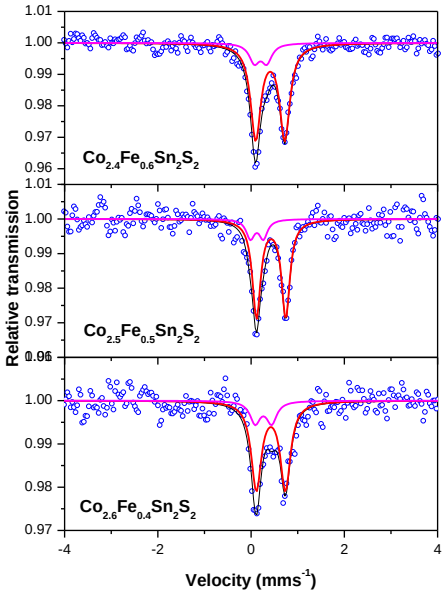

Figure 3 ^{57}Fe Mössbauer spectroscopy data collected at room temperature for three samples of the series $Co_{3-x}Fe_xSn_2S_2$ ($0 \leq x \leq 0.6$). Points denote experimental data and the full lines signify the fit to the two overlapping doublets and the overall fit.

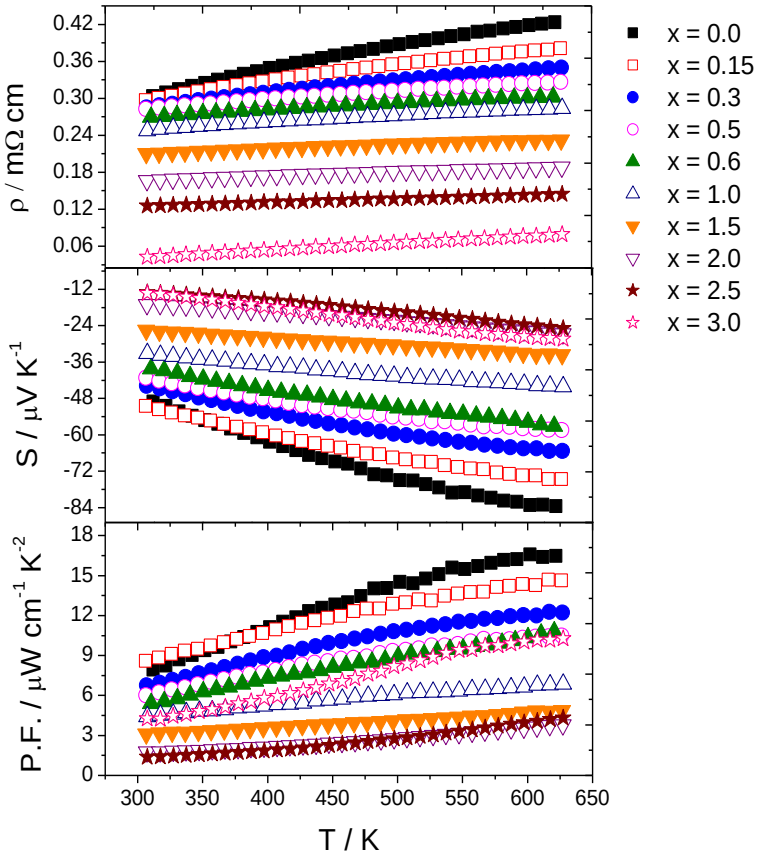

Figure 4 Resistivity, Seebeck coefficient and power factor (PF) data for $Co_{3-x}Ni_xSn_2S_2$ ($0 \leq x \leq 3$).

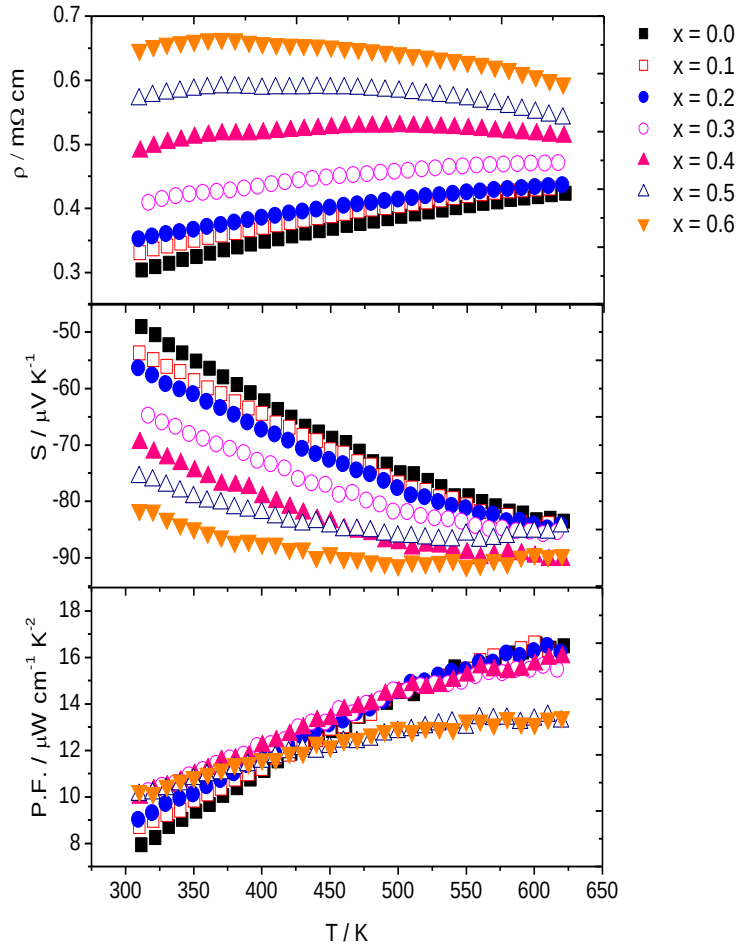

Figure 5 Resistivity, Seebeck coefficient and power factor (PF) data for $Co_{3-x}Fe_xSn_2S_2$ ($0 \leq x \leq 0.6$).

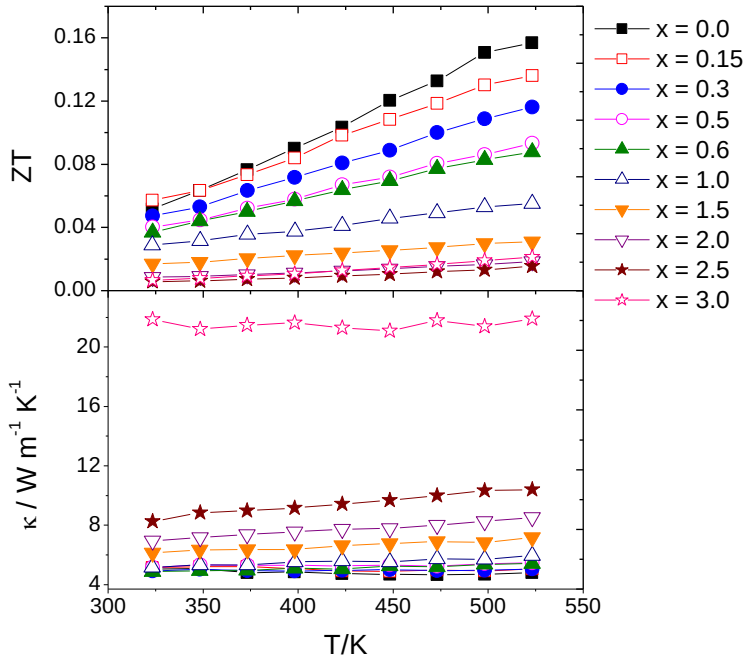

Figure 6 Thermal conductivity data and ZT values of $Co_{3-x}Ni_xSn_2S_2$ ($0 \leq x \leq 3$).

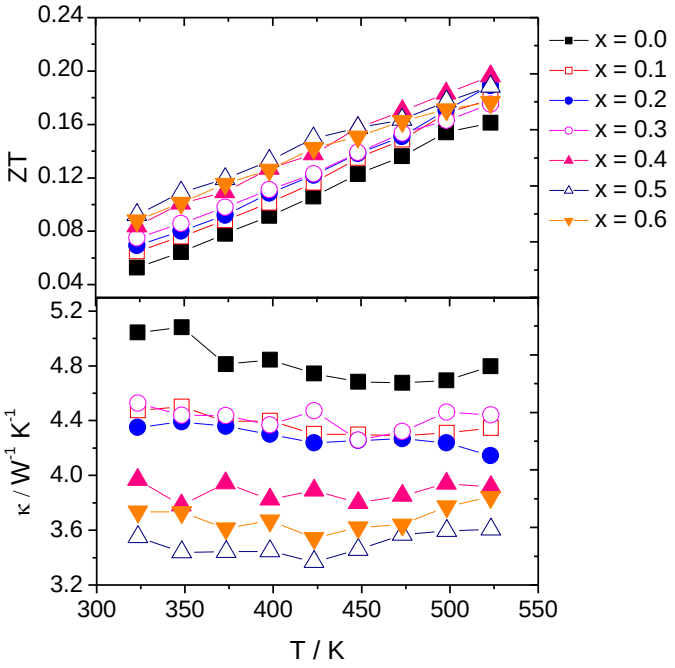

Figure 7 Thermal conductivity data and ZT values of $Co_{3-x}Fe_xSn_2S_2$ ($0 \leq x \leq 0.6$).